



Effect of Ce Microalloying on Microstructure and Mechanical Properties of Extruded Mg–10Gd–0.5Zr Alloy

Laidong Yang^{1,2,3} · Quanan Li^{1,3,4} · Xiaoya Chen^{1,3} · Wanwan Mei^{1,3} · Nana Zhang^{1,3}

Received: 12 December 2022 / Accepted: 13 March 2023 / Published online: 27 March 2023
© The Author(s) under exclusive licence to The Korean Institute of Metals and Materials 2023

Abstract

The influence of Ce microalloying (0.6 wt%) on the microstructure and strengthening mechanism of the extruded Mg–10Gd–0.5Zr alloy were comprehensively researched and analyzed. The experimental results revealed that the addition of 0.6 wt% Ce excellently reduced the grain size of the as-cast alloy and increased the amount of Mg₅Gd eutectic phase. The Ce microalloying promoted the dynamic recrystallization level of the extruded alloy, reduced the number and grain size of deformed grains, increased the number of dynamically recrystallized grains, and transformed the basal plane $\langle 10\bar{1}0 \rangle$ fiber texture gradually into $\langle 0001 \rangle$ texture. Ce microalloying promoted the dynamic precipitation of a small amount of β -Mg₅Gd and α -Mg₁₂Ce particles. After peak aging, the Ce microalloying improved the aging response, increased the aging hardness of the alloy, promoted the aging precipitation of β' phase, and enhanced the quantity and aspect ratio of β' phase. The incremental tensile yield and ultimate tensile strength of the extruded alloy resulting from Ce microalloying are 14 MPa and 11 MPa separately, and those of the peak-aged alloy are 53 MPa and 34 MPa respectively. The increase in yield strength of the extruded and peak-aged alloy is ascribed to the enhanced grain boundary strengthening and the promotion of the β' phase precipitation strengthening by Ce microalloying, respectively.

Keywords Mg–10Gd–0.5Zr alloy · Ce microalloying · Texture · Strengthening mechanism · Microstructure and mechanical properties

1 Introduction

The growing demand for low-density metal engineering materials in the industry has stimulated the research enthusiasm for magnesium (Mg) metal. Mg used as an engineering component can significantly reduce the weight of

construction, and improve the efficiency of energy applications. However, Mg alloy has poor deformation ability and lower strength, which limits its wide application [1, 2, 3]. Among Mg alloys, Mg–Gd-based alloys have attracted much attention due to their excellent mechanical properties [4, 5]. This is due to the generation of dense β' strengthening phase during peak aging treatment, which makes the alloy have excellent strength at room and high temperatures [6, 7, 8]. To further improve the mechanical properties of Mg–Gd-based alloys, alloying and severe plastic deformation (SPD) are two effective methods.

In recent decades, investigators found that adding Y, Sm, and Zn to Mg–Gd alloys can enhance the strength by promoting aging precipitation, grain refinement, or forming the long period stacking order (LPSO) phase, and a series of high-performance Mg–Gd-based alloys have been developed [8, 9, 10, 11]. For example, Liu et al. [10] found that the ultimate tensile strength (UTS) of the Mg–10Gd–2Sm–0.5Zr alloy with Sm addition reached 347 MPa at the peak aging state. The UTS of the extruded Mg–10Gd–2Y–0.5Zr alloy with the addition of Y element reached 390 MPa after peak

✉ Quanan Li
liquanan2016@163.com

✉ Xiaoya Chen
chenxiaoya2010@163.com

¹ School of Materials Science and Engineering, Henan University of Science and Technology, Luoyang 471023, China
² College of Intelligent Manufacturing, Longdong University, Qingyang 745000, China
³ Provincial and Ministerial Co-Construction of Collaborative Innovation Center for Non-Ferrous Metal New Materials and Advanced Processing Technology, Luoyang 471023, China
⁴ Longmen Laboratory, Luoyang 471000, China

aging treatment [8]. However, the total amount of rare earth alloying elements added to these high-performance Mg alloys is essentially more significant than 12 wt%, which not only raises the price but also enhances the weight of the Mg alloy.

Severe plastic deformation (SPD) is used to improve the mechanical properties of Mg alloys by plastic deformation at high strain rates with large strains in order to prepare fine-grain alloys [12, 13, 14, 15, 16, 17]. For example, Tang et al. found that Mg–10Gd–4.8Y–0.6Zr alloy exhibited excellent UTS (336 MPa) and elongation (21%) after 6-passes of multidirectional forging processing [16]. Although the SPD method is capable of producing fine-grained alloys, its complicated process, low efficiency, and high expense make it difficult to be widely applied industrially. Moreover, Wan et al. prepared nanocrystalline Mg–8Gd–3Y–0.4Zr alloy with an average grain size of 80 nm using the rotary swaging technique, and the tensile yield strength (TYS) and UTS of the alloy were 650 MPa and 710 MPa after aging heat treatment, respectively, which is the highest strength bulk Mg alloy known so far [18]. However, the technology is still far from industrial application and needs more effort.

Microalloying is a potential alloying method, and the content of the elements in Mg alloys generally doesn't exceed 1 wt% [19, 20, 21, 22]. Therefore, choosing the right microalloying element will improve the mechanical properties and reduce the cost of Mg alloys. Microalloying elements Sr, Ca, Bi, Ce, La, Ag, and Mn are commonly added to Mg alloys. These elements have been added to Mg alloys individually or in combination to prepare many high-performance Mg alloys [19, 20, 23, 24, 25, 26, 27]. As the cheap of the light RE elements, the addition of trace amounts of Ce to Mg alloys can significantly refine the grain size, weaken the texture, enhance the ductility and improve the mechanical properties [23, 24, 28, 29].

There are few studies on the effects of Ce microalloying on the microstructure and mechanical properties of Mg–Gd–Zr alloys. In this paper, we choose Mg–10Gd–0.5Zr alloy as the target alloy, expecting to substitute the expensive Gd element with a trace amount of Ce, observe the modification of Ce microalloying on the microstructure of Mg–10Gd–0.5Zr alloy, study its effect on the mechanical properties, and analyze the strengthening mechanism. Our work is expected to promote the industrial production of high-performance Mg–Gd–Zr alloys by exploring a simple and low-cost method of Ce microalloying.

2 Material and Methods

The nominal components of the target ingot are Mg–10Gd–0.5Zr (marked GK alloy) and Mg–10Gd–0.6Ce–0.5Zr (marked GK-0.6 alloy). The

actual chemical compositions tested by ICP-AES are summarized in Table 1.

The raw materials containing pure Mg (99.9 wt%), Mg-30 wt% Gd, Mg-30 wt% Ce, and Mg-30 wt% Zr were melted in a resistance furnace with a protective atmosphere (mixed CO₂ and SF₆ gas) at 720 °C for 20 min. Pouring the melt into a steel die. A cylindrical billet with a height of 40 mm and a diameter of 49 mm was processed by electrical discharge machining (EDM). The billet was made homogenized treatment at 525 °C for 12 h and then quenched in hot water. Then, it was preheated at 490 °C for 1 h and backward extrusion was conducted to form an extruded bar with a diameter of 16 mm. The extrusion ratio is about 9:1. The extrusion bars were quenched in hot water after the extrusion. The extruded GK and GK-0.6 samples were subjected to isothermal aging treatment at 225 °C with different hold times.

Microstructure of the alloy observed by field emission scanning electron microscope (FE-SEM, JSM-7800) equipped with a backscatter diffraction probe (EBSD, Oxford Instrument Nordlys) and metalloscope (Zeiss Axio Vert A1). A transmission electron microscope (JEM-2100) and X-ray diffractometer (XRD, Bruker D8) was used for phase identification and structure analysis. The transversal method is used for grain size statistics. The EBSD sample is electropolished and argon polished. EBSD data were collected in steps of 0.7 μm and subjected to analysis using Aztec software. TEM samples were produced by electrolysis double-jet, and the size of the precipitated phase was observed by Digital Micrograph software. Ten pictures were selected to calculate the quantity density and aspect ratio of aging precipitates, and the number density per unit area was estimated using the formula number/area. The dog-bone-like tensile specimens were machined by EDM along the extrusion direction of the bar. The gauge length of the tensile specimen is 15 mm, and the thickness and width are 2 mm and 3 mm, respectively. The tensile test was carried out on the AG-1250KN testing machine at 25 °C. The tensile rate is 1 mm/min. Each specimen is tested three times and calculated the average values.

Table 1 Actual and nominal compositions (wt%) of the target alloys

Alloys	Nominal composition	Gd	Ce	Zr	Mg
GK	Mg–10Gd–0.5Zr	10.36	–	0.29	Bal
GK-0.6	Mg–10Gd–0.6Ce–0.5Zr	10.00	0.51	0.22	Bal

3 Results and Discussion

3.1 Microstructure of as-Cast and Homogenized GK and GK-0.6 Alloys

The optical Microscope (OM) microstructure of as-cast GK and GK-0.6 alloys are displayed in Fig. 1. The morphology of the GK alloy with coarse dendritic grain, and the approximate average grain size (AGS) is 130 μm . After Ce microalloying, the coarse grain reduces significantly, and successive eutectic phases appear between grains. The average size of the grains is approximately 48 μm . This is because the maximum solid solubility of Ce in the Mg is merely 0.74 wt% at 590 $^{\circ}\text{C}$, and it sharply diminishes to almost zero with the decrease in temperature [30, 31]. A mass of Ce atoms tends to concentrate at the tip of the solid–liquid boundary during solidification, giving rise to component undercooling, which increases the undercooling degree. Therefore, the quantity of grains increases, and the size of grains decreases during solidification. Figure 1c and d show the backscatter SEM morphology of as-cast GK and GK-0.6 alloys. The GK alloy shows a typical as-cast microstructure. After adding 0.6 wt% Ce, many intermetallic particles appear at the grain boundary, which is consistent with the characteristics in the OM images.

The XRD patterns of as-cast GK and GK-0.6 alloys are shown in Fig. 2. There is the peak of the α -Mg matrix, and no peaks of other intermetallic compounds are observed in the GK alloy. After Ce microalloying, in addition to

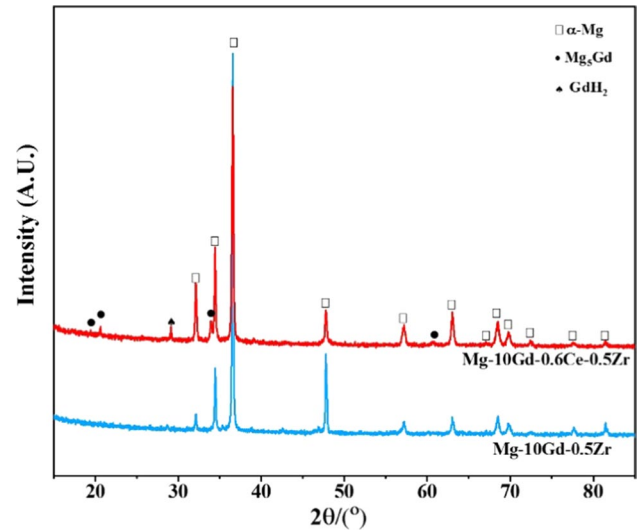
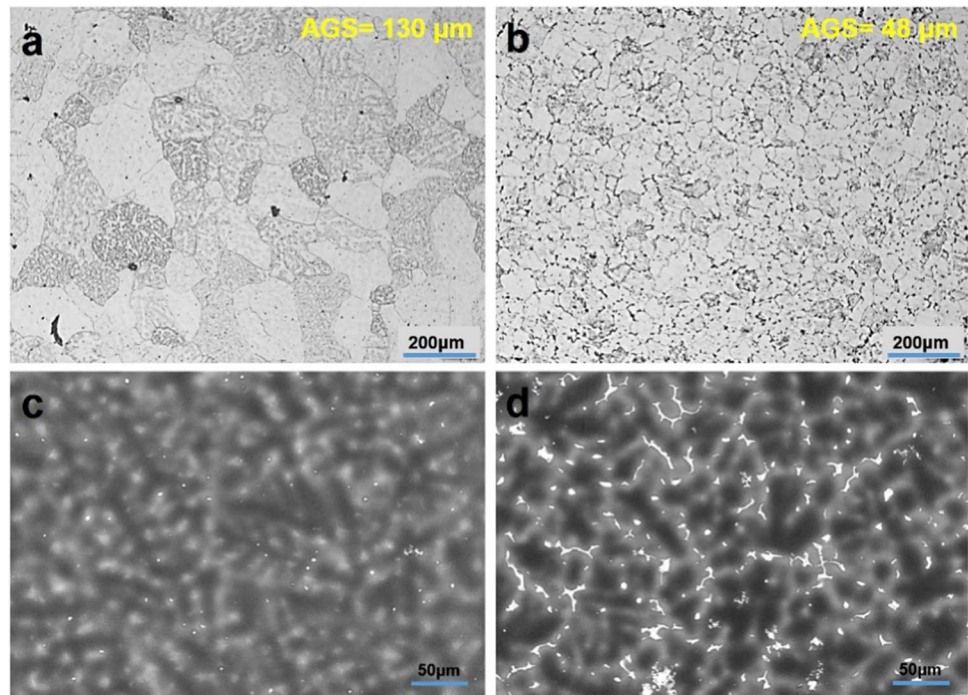


Fig. 2 XRD patterns of the as-cast GK and GK-0.6 alloys

the peak of Mg, the peak of the β -Mg₅Gd (FCC structure, $a = 2.22$ nm [32]) appears in the GK-0.6 alloy. Furthermore, a particular peak appears near 28 $^{\circ}$, which neither belongs to the β -Mg₅Gd phase nor belong to any Ce-containing intermetallic phase. Zheng and Peng et al. [33, 34] considered that the particular peak was the GdH₂ phase (FCC structure, $a = 0.53 \sim 0.56$ nm). The GdH₂ phase was easy to appear in Mg alloy during casting and thermal treatment. Zhu et al. [35] suggested that hydrogen atoms participated in the decomposition of Mg–Gd eutectic

Fig. 1 OM and backscatter SEM micrographs of the cast GK a, c and GK-0.6 alloy b, d



compounds, which may produce the RE hydride during the casting process and thermal treatment.

After Ce microalloying, a mass of the eutectic compound is generated at the grain boundary. To comprehensively study the crystalline structure of the compound, the cast GK-0.6 alloy was characterized by TEM. Figure 3 displays the BF-TEM morphology and the corresponding selected area electron diffraction (SAED) patterns of the eutectic phase of the alloy. Two black eutectic compounds are generated at the grain boundaries, which appear similar to triangles (Fig. 3a) and reticulations (Fig. 3c), respectively. The corresponding SAED patterns show that the eutectic phase of both forms is a β -Mg₅Gd phase. There is no found Mg₁₂Ce phase in the GK-0.6 alloy. Therefore, Ce microalloying significantly promotes the generation of the β -Mg₅Gd eutectic compound in the GK-0.6 alloy.

After homogenization treatment of the as-cast GK and GK-0.6 alloys, the dendrites of the alloys disappeared and

exhibited equiaxed grains (Fig. 4). As seen in Fig. 4b, the microstructure of the homogenized alloy was significantly refined after Ce microalloying, and its average grain size (AGS) reduced from 121.3 to 77.8 μ m.

3.2 Microstructure of Extruded GK and GK-0.6 Alloys

Figure 5 is the longitudinal SEM images of extruded GK and GK-0.6 alloys and the corresponding element and point EDS mappings; After extrusion, there are extrusion stringers dispersed along the extrusion direction in GK alloy. These stringers are second-phase particles that are diffusely distributed during extrusion (Fig. 5a). Based on element mappings and point EDS analysis, these particles are mainly Zr-rich insoluble particles and a small amount of Gd-rich intermetallic particles. Larger particles (labeled A) and smaller particles (labeled D) in Fig. 5a are mainly Gd-rich phases,

Fig. 3 BF-TEM **a, c** and corresponding SAED patterns **b, d** of as-cast GK-0.6 alloy

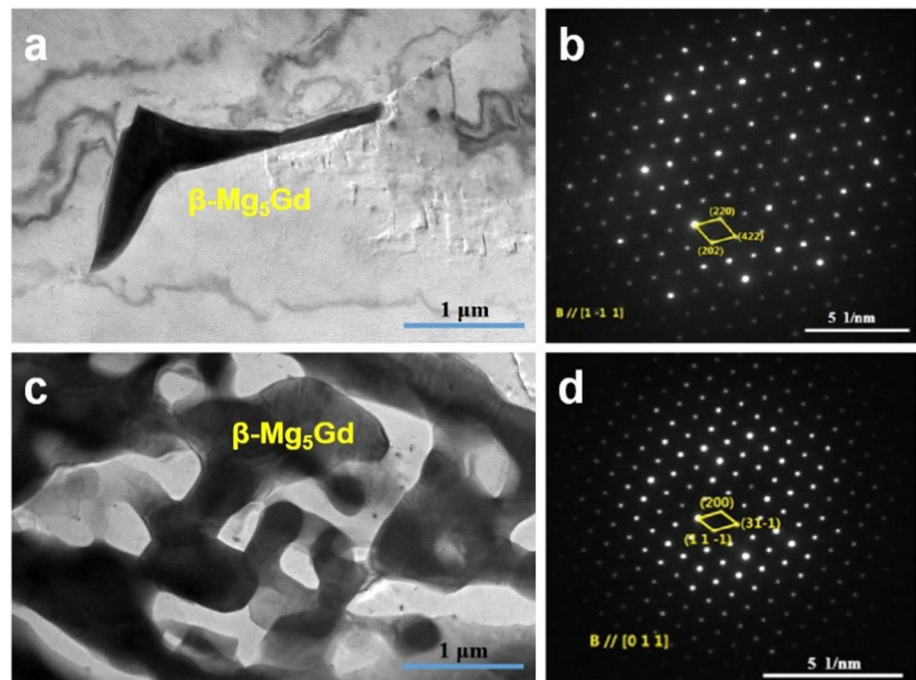
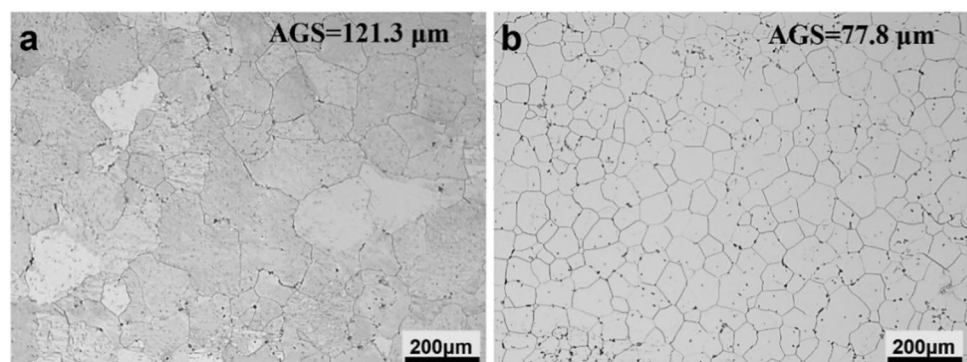


Fig. 4 OM micrographs of the GK **a** and GK-0.6 alloys **b** after homogenized treatment



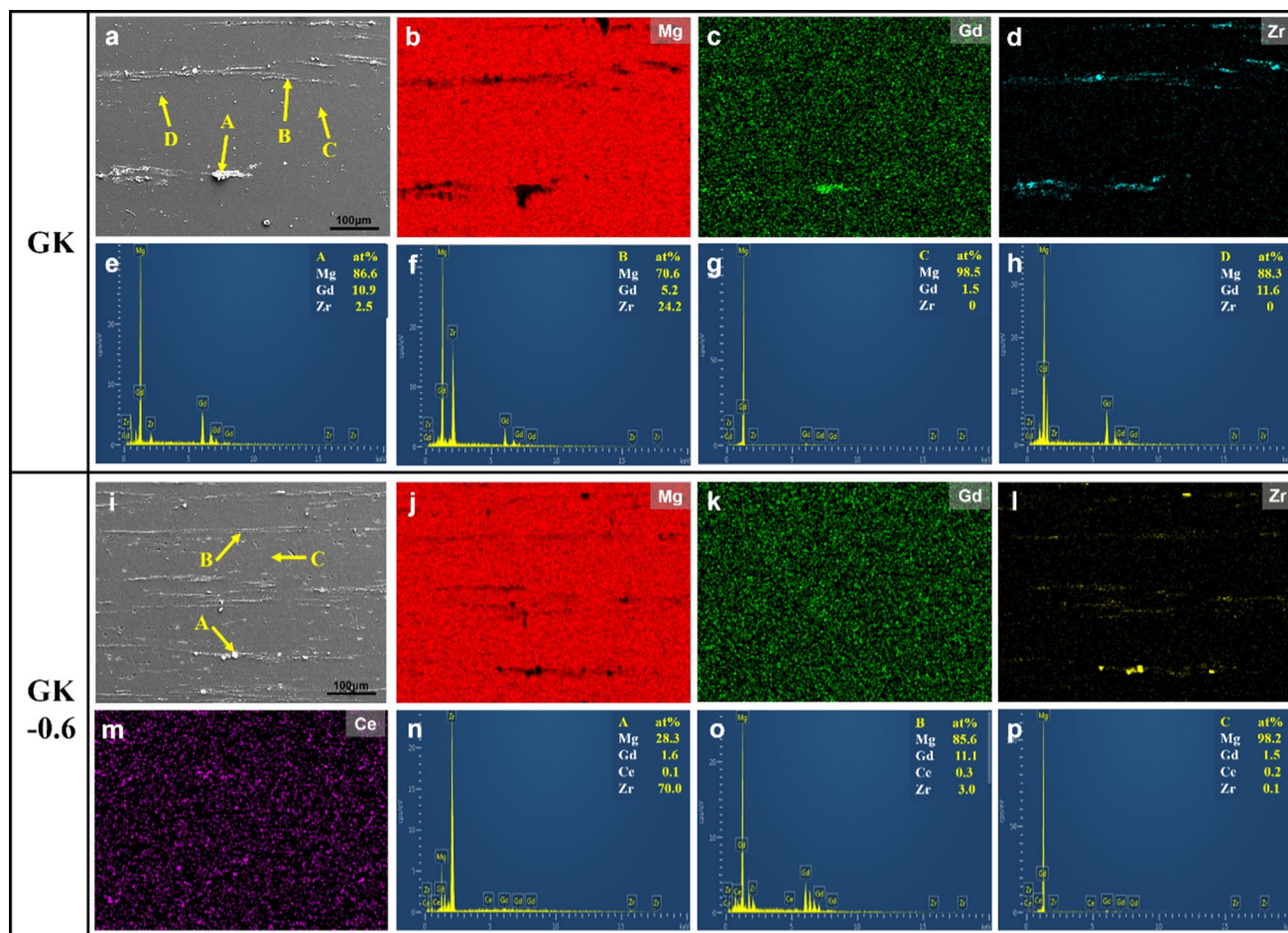


Fig. 5 SEM micrographs, and element and the point EDS mappings of extruded GK and GK-0.6 alloy

probably the unfused β - Mg_5Gd phase and Gd_2H phase, while the fine particles (labeled B) contain a high concentration of Zr, which are insoluble Zr particles; The proportion of Gd in the completely solid solution grains (labeled C) is about 1.5 at%, indicating that most of Gd are uniformly dissolved into the grains of GK alloy. Compared with GK alloy, the number of the extruded stringers along the extrusion direction increases significantly in GK-0.6 alloy (Fig. 5i). Similar to GK alloy, these second phases are mainly composed of Gd-rich and Zr-rich particles, possibly unfused Zr-rich particles, and the β - Mg_5Gd phase or GdH_2 phase.

OM micrographs of the transverse and longitudinal sections of the two the extruded alloys are demonstrated in Fig. 6. Both alloys possess bimodal structure, which consists of a great deal of small recrystallized grains and large deformed grains with a strip shape. The deformed grains in GK alloy are larger in size and number, and with a volume fraction of about 27%. After Ce microalloying, the proportion of recrystallized grains is markedly improved, and the grain size and the number of deformed grains is obviously decreased, with a volume fraction of about 15%. This

indicates that Ce microalloying can prominently promote the recrystallization of the extruded GK alloy.

Figure 7 displays the inverse pole figure (IPF) maps of two the extruded alloys. To research the influence of Ce microalloying on the recrystallization, grain orientation spread (GOS) was applied to split grains into deformed grains ($GOS \geq 2^\circ$) and dynamically recrystallized (DRXed) grains ($GOS < 2^\circ$) [36, 37]; The size (length, width) and the number of deformed grains decrease sharply, but the number of fine DRXed grains increase apparently after Ce microalloying.

Therefore, the dynamic recrystallization (DRX) process of the extruded alloy can be well promoted by Ce microalloying, which corresponds with the results of Fig. 6. Imandoust et al. [38] believed that the Ce element has a stronger tendency to promote dynamic recrystallization than the Gd element. The addition of 0.6 wt% Ce resulted in a large number of broken particles during extrusion, which helped to provide nucleation sites for dynamically recrystallized grains, further promoting dynamic recrystallization through particle stimulated nucleation (PSN) mechanism [23, 39].

Fig. 6 OM images of transverse **a, b** and longitudinal sections **c, d** of extruded GK **a, c** and GK-0.6 **b, d** alloys

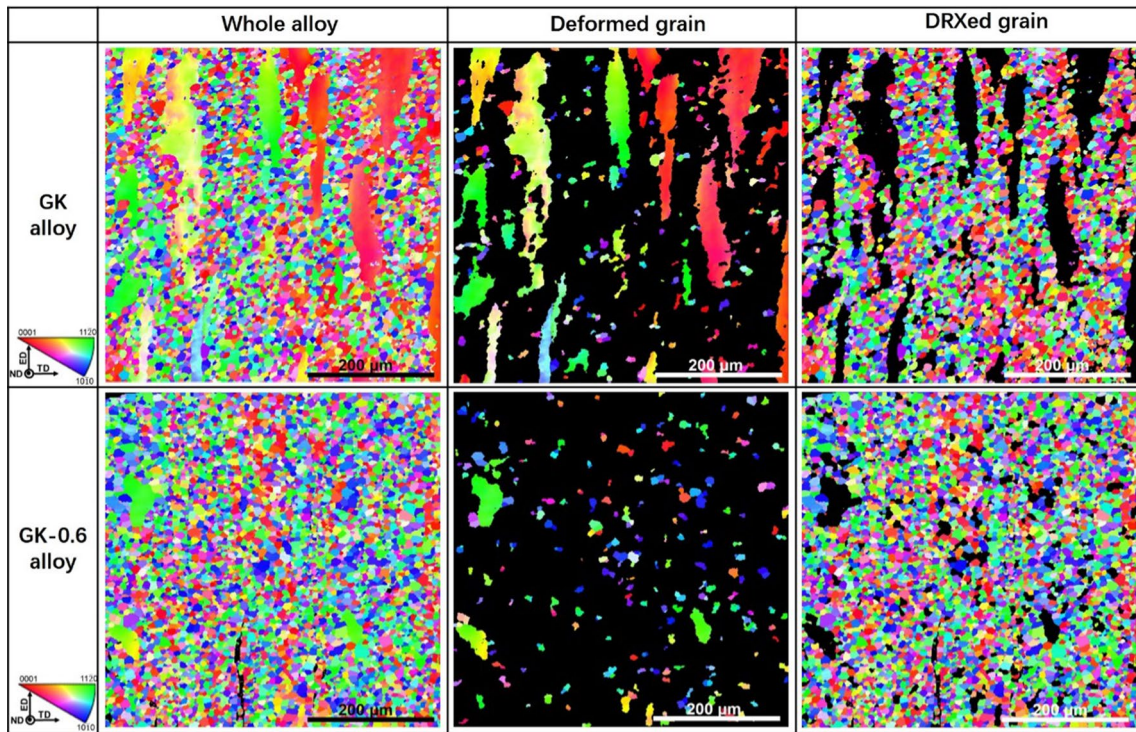
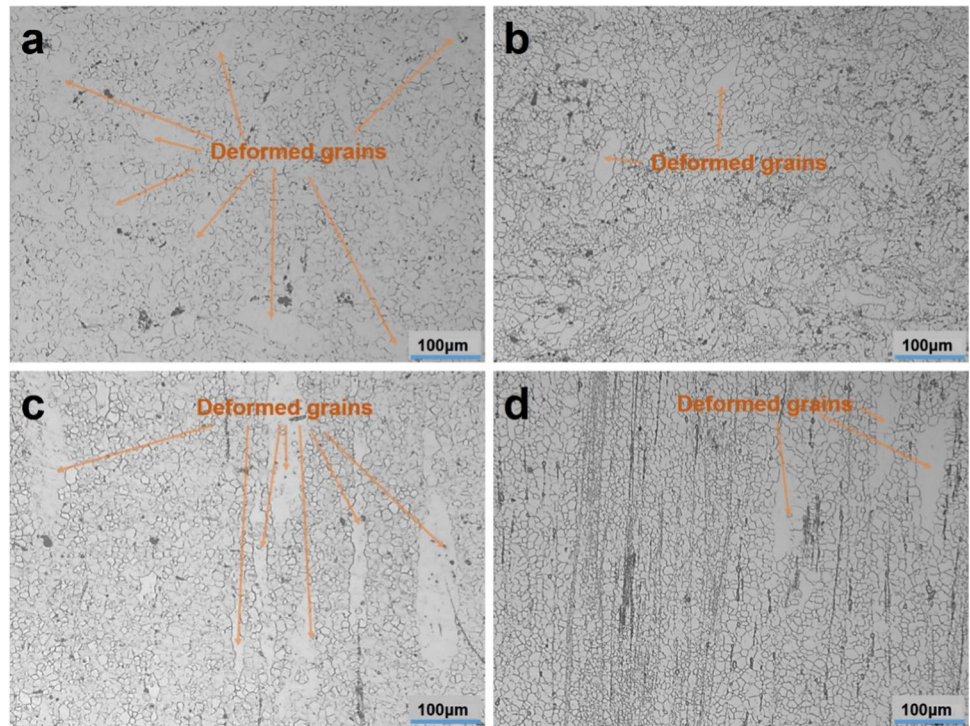


Fig. 7 IPF maps of the extruded GK and GK-0.6 alloys

Hui et al. [40] found that the addition of Ce promoted the DRX of the extruded ZK60 alloy through a PSN mechanism. It was also suggested that the local stress concentration around the Mg–Zn–Ce particles in the coarse deformed grains increased during extrusion, and generating the storage energy reached the threshold for triggering DRX and increasing the volume fraction of DRXed grains.

Figure 8 demonstrates the extruded GK alloy has a $\langle 10\bar{1}0 \rangle // \text{ED}$ extruded direction (ED) fiber texture that appeared commonly in extruded Mg–RE alloy, and the texture intensity is 4.0. The extruded GK alloy has a prominent bimodal structure. Its coarse deformed grains have an intense $\langle 10\bar{1}0 \rangle // \text{ED}$ fiber texture and its texture intensity is up to 11.7, while the DRXed grains possess a comparatively weak and random texture, and the texture intensity is only 1.8; Moreover, the Ce microalloying significantly promotes the dynamic recrystallization, and the $\langle 10\bar{1}0 \rangle // \text{ED}$ texture of the GK alloy progressively changes into a weak $\langle 0001 \rangle // \text{ED}$ abnormal texture of the GK-0.6 alloy, and the texture strength decreases from 4.0 to 3.2.

The initial grains in the GK-0.6 alloy rotate continuously during extrusion deformation, gradually producing coarse deformed grains with strong $\langle 10\bar{1}0 \rangle // \text{ED}$ orientation, some of the deformed grains with smaller grain sizes produce $\langle 0001 \rangle // \text{ED}$ reorientation. This causes the deformed grains of the alloy to exhibit $\langle 10\bar{1}0 \rangle$ and $\langle 0001 \rangle$ double-fiber textures, and the texture strength is reduced from 11.7 to 4.9. After Ce microalloying, the fine DRXed grains of the alloy shows a $\langle 0001 \rangle // \text{ED}$ abnormal orientation, and the texture strength increase from 1.8 to 3.0. Therefore, the Ce microalloying promotes the DRX process of Mg–10Gd–0.5Zr alloy, transforms the $\langle 10\bar{1}0 \rangle // \text{ED}$ fiber texture to $\langle 0001 \rangle // \text{ED}$ texture, and weakens the texture.

Abnormal $\langle 0001 \rangle // \text{ED}$ texture in hot-extruded Mg–RE alloy has also been reported [41, 42, 43, 44]. Lyu et al. [41] believed that the $\langle 0001 \rangle // \text{ED}$ orientation of the extruded MMg–7Y–5Sm–0.5Zn–0.3Zr alloy was related to the high RE concentration and large strain; Alizadeh et al. [42] considered that when the RE element concentration and extrusion ratio are large, the extruded Mg–9Gd–4Y–0.4Zr alloy produced an unusual $\langle 0001 \rangle // \text{ED}$ texture, and proposed that the large extrusion ratio provided the energy required for the DRX process. And the high RE concentration promoted the non-basal slip and the solute drag to make the DRXed grains grow preferentially, and finally formed the $\langle 0001 \rangle // \text{ED}$ texture. The DRXed grains of the Mg–6Gd–4Y–0.5Zn–0.5Zr alloy showed obvious $\langle 0001 \rangle // \text{ED}$ texture through continuous dynamic recrystallization (CDRX) mechanism and non-basal slip at high extrusion temperature and extrusion ratio [43]. It suggested that static recrystallization and preferential growth are not responsible for this abnormal texture, which is related to the DRX process facilitated by non-basal slip. Kim et al. [44] found that the extruded binary Mg–Gd alloys formed $\langle 0001 \rangle // \text{ED}$ texture when the Gd concentration was extended to 15 wt%. It is inferred that the high concentration of RE atoms at the grain boundary led to the abnormal orientation. To sum up, in this paper, the DRXed grains of the GK-0.6 alloy form an obvious $\langle 0001 \rangle // \text{ED}$ abnormal texture, and the texture strength increased from 1.8 to 3.0 after Ce microalloying. The trace Ce significantly promotes the development of this abnormal texture. The atomic radius of Ce and Gd atoms are 0.182 nm and 0.180 nm, which are much greater than the atomic radius of Mg with 0.16 nm, and Ce's atomic radius is also greater than that of Gd. Hence, the large radius and small diffusion

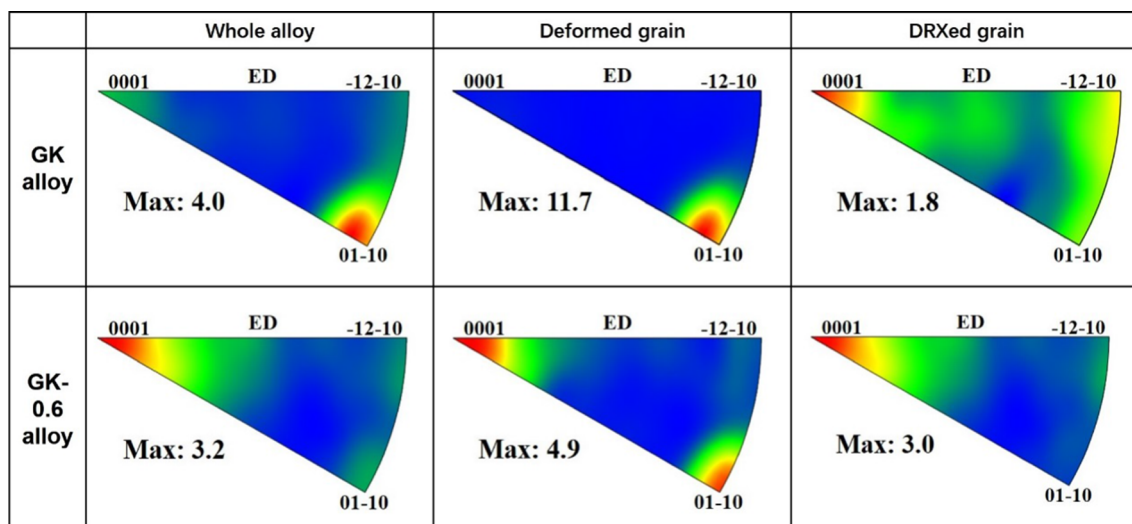


Fig. 8 IPF of the extruded GK and GK-0.6 alloys

rate of Ce and Gd atoms, leading to the RE solutes being aggressively segregated at the grain boundaries. The solute drag effect hinders grain boundary migration and dislocation movement, gradually activating non-basal slip and producing an <0001> //ED abnormal texture.

As seen from the XRD patterns of the extruded GK and GK-0.6 alloys (Fig. 9), both alloys exhibit mainly strong diffraction peaks of the Mg matrix, while the intensity of the (0002) and (10 $\bar{1}$ 0) plane diffraction peaks change dramatically after Ce microalloying. The intensity of the (10 $\bar{1}$ 0) peak of extruded GK alloy is the largest, while that of the (10 $\bar{1}$ 0) peak of the extruded GK-0.6 alloy decreases sharply, and that of the (0002) peak increases. The

diffraction intensities of (0002) and (10 $\bar{1}$ 0) planes of the two alloys after normalization are compared using Eqs. (1) and (2), which also reveals a change in the texture of the extruded alloy after Ce microalloying [45], which is also consistent with the conclusion in Fig. 8.

$$\frac{I_{(10\bar{1}0)_A}}{I_{(0002)_A}} = 2.5 \tag{1}$$

$$\frac{I_{(10\bar{1}0)_B}}{I_{(0002)_B}} = 0.64 \tag{2}$$

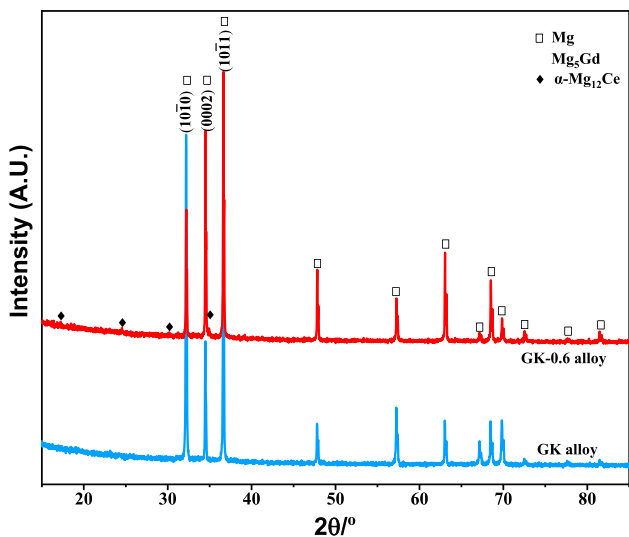
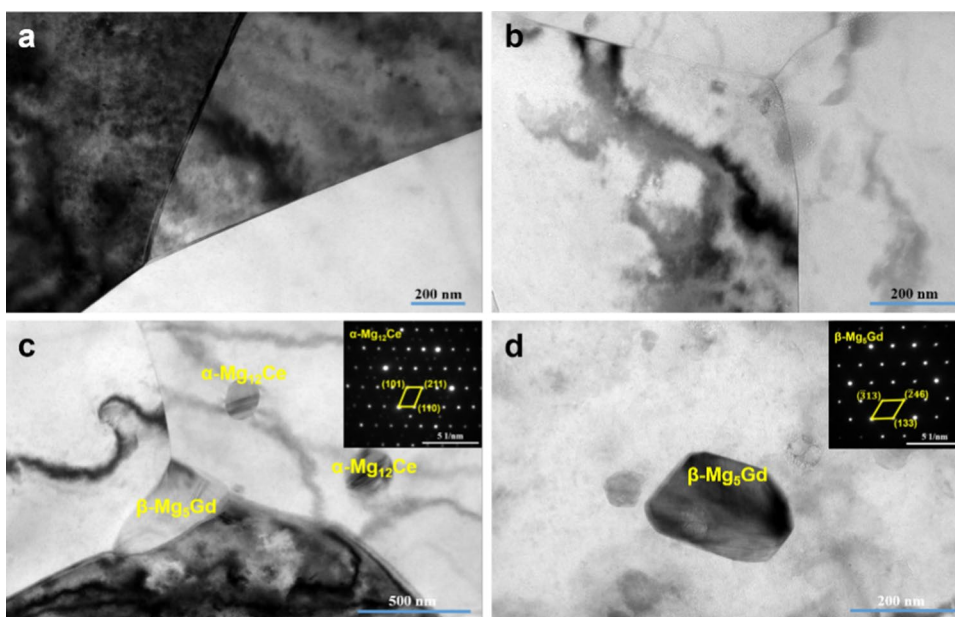


Fig. 9 XRD patterns of the extruded GK and GK-0.6 alloys

After Ce microalloying, besides the diffraction peak of the Mg matrix, there are other diffraction peaks with very low intensity on the XRD pattern of the GK-0.6 alloy. These may be the peaks of β -Mg₅Gd and Mg₁₂Ce phases after analysis. These weak diffraction peaks do not appear in the XRD pattern of the GK alloy, indicating that some new compounds were produced after the addition of Ce.

Figure 10 demonstrates the BF-TEM morphology of the extruded GK and GK-0.6 alloys. Figure 10a and b indicate that there are no dynamically precipitated nanoparticles found inside grains of the GK alloy. A few nano-spherical precipitated particles are produced adjacent to the grain boundaries of the extruded GK-0.6 alloy. The size of the nano-precipitate is about ~500 nm. A litter number of nano-precipitates with a size of about 100–200 nm also appear inside grains. Li and Zhang et al. [23, 46] indicated that there are two types Mg₁₂RE phases in Mg-RE-based alloys, namely α -Mg₁₂RE (bct structure, a = 11.33 Å and c = 5.96 Å)

Fig. 10 BF-TEM morphology and SAED patterns of extruded GK a, b and GK-0.6 c, d alloys



and β -Mg₁₂RE (bct structure, $a = 10.33 \text{ \AA}$ and $c = 77.50 \text{ \AA}$). Using SAED analysis of these precipitated particles, it is found that the nanoparticles in the extruded GK-0.6 alloy are β -Mg₅Gd and α -Mg₁₂Ce phase particles, which correspond with the XRD patterns in Fig. 9. Therefore, it is inferred that Ce microalloying promotes dynamic precipitation, and a small amount of β -Mg₅Gd and α -Mg₁₂Ce nanoparticles are precipitated inside the grain and at the grain boundary.

3.3 Microstructure of Extruded GK and GK-0.6 Alloys During Peak Aging

The curves of the extruded alloy isothermal aging at 225 °C are demonstrated in Fig. 11. After Ce microalloying, the hardness value of the extruded alloy increases rapidly from

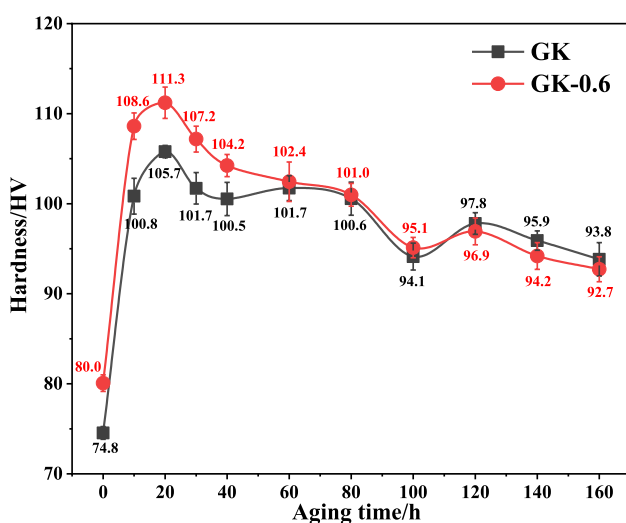


Fig. 11 Isothermal age hardening curves of the GK and GK-0.6 alloys

74.8 HV to 80 HV. Both alloys reach peak aging at 20 h simultaneously. At the peak aging, the hardness value of the GK-0.6 alloy (111.3 HV) is higher than that of the GK alloy (105.7 HV). The Ce microalloying promotes the aging precipitation and increased the age-hardening response.

Figure 12 exhibits BF-TEM microstructures of the alloys after peak aging observed from $[0001]_{\text{Mg}}$ and $[11\bar{2}0]_{\text{Mg}}$ axes. A great quantity of plate-like nanoparticles are generated after peak aging, which are determined to be β' phase (cbco structure, $a = 0.65 \text{ nm}$, $b = 2.27 \text{ nm}$, $c = 0.52 \text{ nm}$) [32]. In general, the β' phase is the strengthening phase of the Mg-Gd-based alloy [47]. After peak aging treatment, β' phase is also precipitated in the GK-0.6 alloy. Compared with the GK alloy, β' phase has a higher number density per unit area in the GK-0.6 alloy. Moreover, after Ce microalloying, the average basal plane diameter and thickness of the plate-like β' phase decreased at the same time as observed from the $[0001]_{\text{Mg}}$ axis, and the size of the thickness direction dropped more sharply, resulting in the decrease of the mean area of single β' particles on the $\{0001\}_{\text{Mg}}$. The β' particle produces on three $\{11\bar{2}\}$ prismatic planes exhibits a triangular arrangement on the $\{0001\}_{\text{Mg}}$, and the angle is about 120° [32]. Therefore, all variants of the β' phase on the three prismatic are observed under the $[0001]_{\text{Mg}}$ axis, as shown in the inset in Fig. 12d and h, with a more complex electron diffraction patterns.

Statistical analysis of the β' phase was carried out after peak aging. It is found that the aspect ratio of the β' phase increase from 3.2 to 3.6 after Ce microalloying (Fig. 13a). The number density of β' phase of the GK alloy is about $3.3 \times 10^{14}/\text{m}^2$ (Fig. 13b). The quantity of β' phase enhanced sharply after Ce microalloying, and the area density increased to about $8.7 \times 10^{14}/\text{m}^2$ (Fig. 13b). Therefore, the Ce microalloying significantly enhances the aging

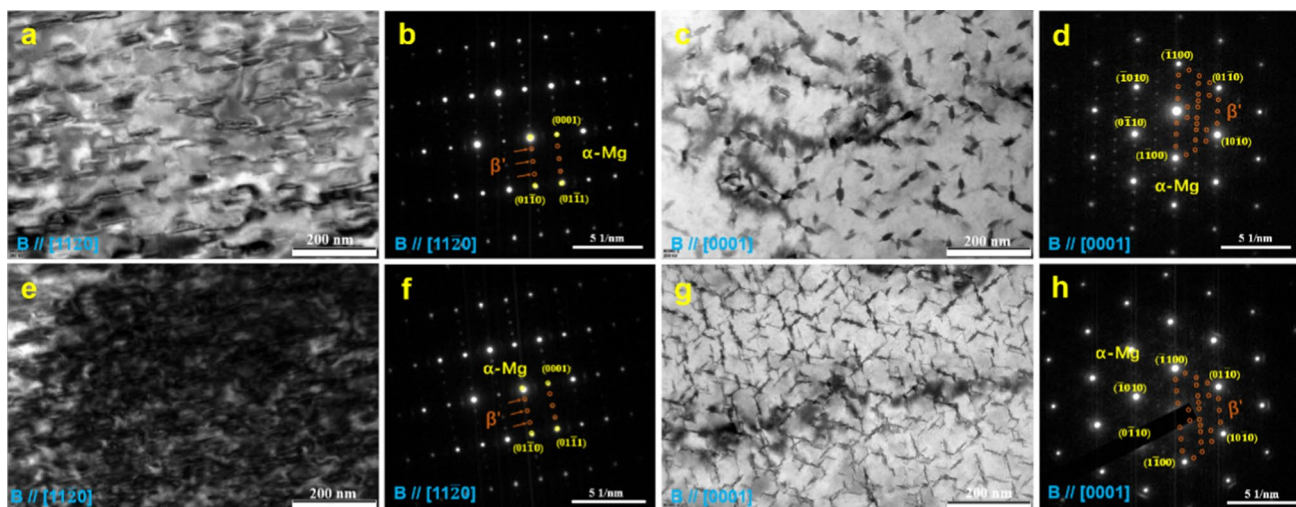


Fig. 12 BF-TEM images a, c, e, g and the corresponding SAED patterns b, d, f, h of GK a, b, c, d and GK-0.6 e, f, g, h alloy at peak aging

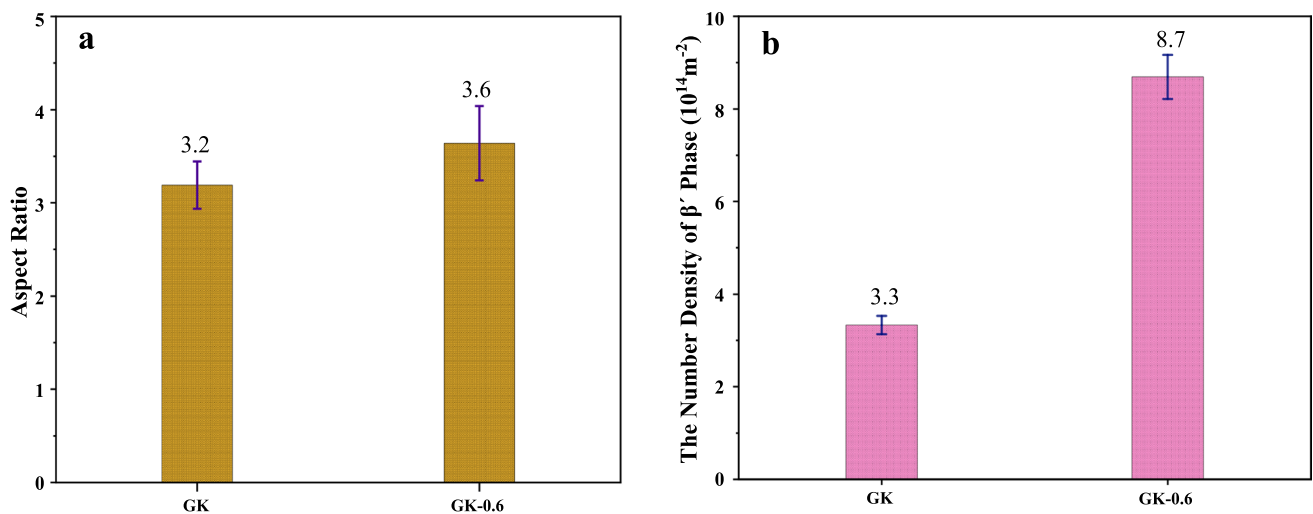


Fig. 13 Aspect ratio **a** and number density **b** of β' particles in GK and GK-0.6 alloys

response of the alloy, and visibly facilitates the precipitation of the β' phase. The solid solubility of Gd in Mg is comparatively large, with a maximum value of 23.49 wt% at 548 °C, and reduces gradually with decreasing temperature [32]. The solid solubility of Ce in the Mg is very small, with a maximum value of 0.74 wt% at 590 °C, and decreases sharply with decreasing in temperature [30, 31, 48]. The lattice distortion of the alloy is significantly increases after Ce microalloying, and the concentration gradient of RE solute in the grain of the extruded GK-0.6 alloy is significantly higher than that of the GK alloy, which provides a greater driving force for the aging precipitation process and allows the formation of a denser β' particles during aging treatment. Due to the large concentration gradient of RE solute atoms in extruded GK-0.6 alloy, the Gd and Ce atoms only need

to move a small distance to meet the concentration required for nucleation and growth of the β' phase during the peak aging when the β' phase rich in (Gd, Ce) elements is formed. Therefore, the β' phase in GK-0.6 alloy is smaller in size and larger in quantity. This is the reason why Ce microalloying improves the aging ability of the GK-0.6 alloy.

3.4 Mechanical Properties and Strengthening Mechanism

Figure 14 displays the tensile mechanical properties of the GK and GK-0.6 alloys in the extruded (a) and peak-aged (b) state. After Ce microalloying, the TYS and UTS of the alloy are obviously enhanced, while the elongation (El) decreases. The mechanical properties calculated from the

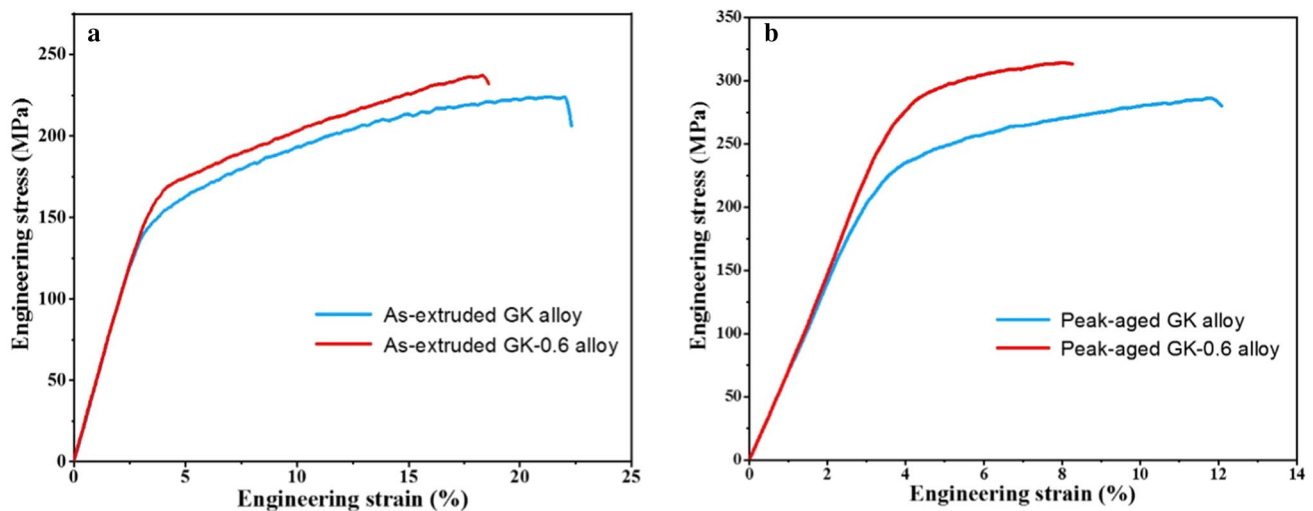


Fig. 14 Stress–strain curves of extruded **a** and peak-aged **b** GK and GK-0.6 alloys

Table 2 Mechanical properties of GK and GK-0.6 alloys in the extruded and peak-aged states

Alloy	Process state	TYS/MPa	UTS/MPa	El/%
GK	Extrusion	135	224	21.0
GK-0.6	Extrusion	149	235	18.2
GK	Extrusion+T5	214	284	12.7
GK-0.6	Extrusion+T5	267	318	8.0

tensile curves of the two alloys in the extruded and peak-aged states, including TYS, UTS, and El, are shown in Table 2. The addition of 0.6 wt% Ce increased the TYS and UTS of the extruded alloy by 14 MPa and 11 MPa, respectively, while the TYS and UTS of the alloy in the peak-aged state increased by 53 and 34 MPa, respectively.

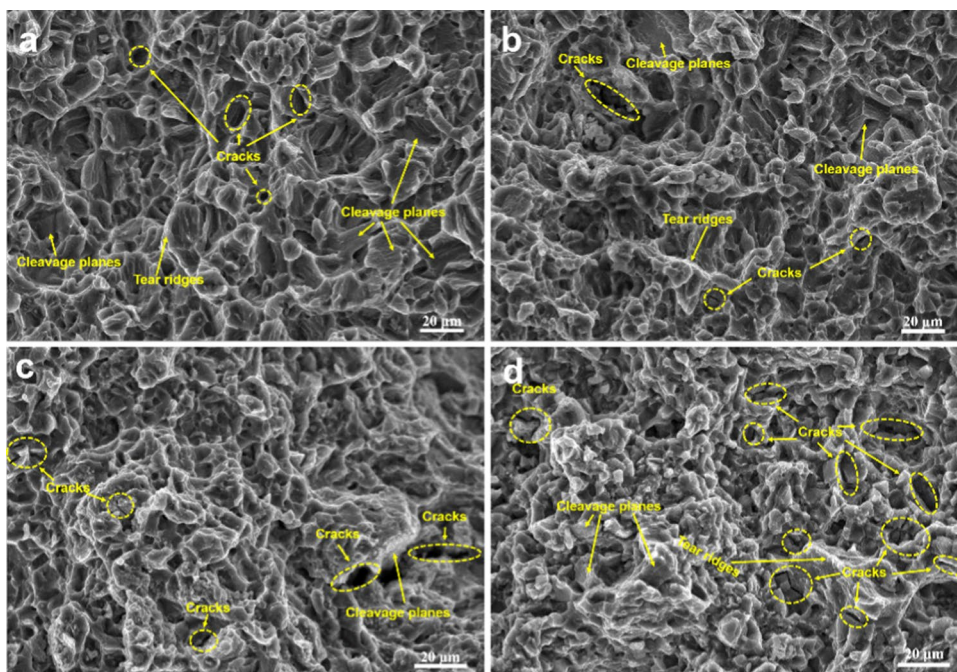
The fracture behavior is usually associated with the microstructure of the fracture surface. Figure 15 shows secondary electron SEM images of the tensile fracture surface of the GK and GK-0.6 alloys in the extruded and peak-aged state. Micro-cracks, cleavage planes, and tear ridges are observed in both extruded GK and GK-0.6 alloys, which indicate the quasi-cleavage brittle fracture characteristics. After peak aging treatment, the number of cleavage planes and tear ridges decreased significantly and the number of micro-cracks increased for both alloys, showing cleavage brittle fracture. However, the number of microcracks in the GK-0.6 alloy is larger than that in the GK alloy, which significantly reduces the elongation of the peak-aged GK-0.6 alloy.

The strengthening mechanism of extruded alloys is mainly grounded on dispersion strengthening ($\Delta\sigma_{ds}$) of dynamically precipitated particles and RE element (Gd, Ce) solution strengthening ($\Delta\sigma_{ss}$), and grain boundary strengthening ($\Delta\sigma_{gbs}$). Due to the small number of dynamically precipitated β -Mg₅Gd and α -Mg₁₂Ce nanoparticles generated in the GK-0.6 alloy after extrusion, the dispersion strengthening effect of the nanoparticles on the alloy can be ignored. The concentration of the Gd element in GK and GK-0.6 alloys is almost the same, and Gd has the same solution strengthening effect on GK and GK-0.6 alloys. Although the solid solubility of Ce in Mg is extremely small, its strengthening on GK-0.6 alloys is related to the atomic fraction of Ce in the alloy. Considering the solid solubility of Ce in Mg, the atomic fraction of Ce in the extruded GK-0.6 alloy was estimated to be 0.014 at%. Therefore, the TYS of the extruded alloy increased by solution strengthening ($\Delta\sigma_{ss}$) of Ce atom after Ce microalloying is calculated by the following formula [49]:

$$\Delta\sigma_{ss} = mB_n C^n$$

where m is Taylor orientation factor, which is a constant, and m equals 5. n is a constant, and $n=2/3$. B is the solute strengthening rate, it equals 39.5 MPa (at.)^{-2/3}. C is the atomic concentration of Ce. After Ce microalloying, the increase in yield strength ($\Delta\sigma_{ss}$) of the extruded alloy is estimated to be 11 MPa due to solution strengthening.

Grain boundary strengthening (σ_{gbs}) is a meaningful approach to promote the strength of Mg alloys by impeding the dislocation movement through grain boundaries.

Fig. 15 SEM images of fracture surface of the extruded **a, b** and peak aging **c, d** of the GK **a, c** and GK-0.6 **b, d** alloys

The TYS of the alloy contributed by the grain boundary strengthening mechanism is estimated using the Hall–Petch relationship as follows [50]:

$$\sigma_{gbs} = \sigma_0 + kd^{-1/2} \tag{3}$$

where d is the average grain size, and k is the Hall–Petch constant [51]. Since Mg alloy has low symmetry, few slip systems, and a large k constant, the grain boundary strengthening is very effective [52, 53]. The extruded GK and GK-0.6 alloys show bimodal structures, so both deformed and fine recrystallized grains contribute to grain boundary strengthening. The yield strength increased by grain boundary strengthening ($\Delta\sigma_{gbs}$) estimate using this equation as follows [54]:

$$\Delta\sigma_{gbs} = f_{unDRX}\Delta\sigma_{unDRX} + f_{DRX}\Delta\sigma_{DRX} \tag{4}$$

where f_{unDRX} and f_{DRX} are the proportion of deformed (unDRXed) grains and DRXed grains of the extruded alloys, respectively. The σ_{unDRX} and σ_{DRX} are the contributions of deformed grains and DRXed grains to grain boundary strengthening, respectively. The contributions of DRXed grains ($\Delta\sigma_{DRX}$) and deformed grains ($\Delta\sigma_{unDRX}$) to yield strength were estimated by the following formula:

$$\Delta\sigma_{unDRX} = k_{unDRX}d_{unDRX}^{-1/2} \tag{5}$$

$$\Delta\sigma_{DRX} = k_{DRX}d_{DRX}^{-1/2} \tag{6}$$

where d_{unDRX} and d_{DRX} are the average grain sizes of deformed grains and DRXed grains, and k is a constant. It is generally 188 MPa $\mu\text{m}^{1/2}$ in wrought magnesium alloys [51, 55, 56]. Table 3 lists the contribution to the TYS of each alloy by grain boundary strengthening. Therefore, the calculated grain boundary strengthening values of the extruded GK and GK-0.6 alloys are 68 and 74 MPa severally. That is, the grain boundary strengthening produced by Ce microalloying increases the TYS of the extruded alloy by 6 MPa. Therefore, the sum of the contribution to the TYS of the extruded alloy by the solution strengthening ($\Delta\sigma_{ss}$) and grain boundary strengthening ($\Delta\sigma_{gbs}$) after Ce microalloying is

about 17 MPa, which corresponds to the increment of the experimental value (14 MPa).

Many dense β' nanoparticles appear in both GK and GK-0.6 alloys after peak aging. Due to the small number of dynamically precipitated β -Mg₅Gd and α -Mg₁₂Ce nanoparticles, the contribution of the nanoparticles to the strength of the aged alloy is negligible, and only the strengthening of β' on the GK and GK-0.6 alloy is considered. After Ce microalloying, the number density of β' phase enhances rapidly, and its size (diameter and thickness) decreases, while the aspect ratio increases. The β' precipitated in the {11–20} prismatic plane contribute to the yield strength of the peak-aged alloys through the Orowan precipitation strengthening ($\Delta\sigma_{ps}$) mechanism. Nie et al. revised the Orowan mechanism of the precipitated phase in the prismatic plane as follows [57]:

$$\Delta\sigma_{ps} = \frac{Gb}{2\pi\sqrt{1-\nu}\left(0.825\sqrt{\frac{d_t}{f}} - 0.393d_t - 0.886t_t\right)} \times \ln \frac{0.886\sqrt{d_t t_t}}{b} \tag{7}$$

where $\Delta\sigma_{GKps}$ and $\Delta\sigma_{GK-0.6ps}$ are the yield strengths of GK and GK-0.6 alloys contributed by the Orowan mechanism of β' phase, b is the Burgers vector ($b=0.32$ nm [29, 58]), ν is the Poisson ratio ($\nu=0.35$ [56]), G is the Mg' shear modulus ($G=16.6$ GPa [29]), and d_t and t_t are the average length and thickness of the cross-section between β' particles and the basal plane, respectively. In this paper, f is the volume fraction of β' phase, which is estimated at 2.76×10^{-2} and 2.85×10^{-2} in GK and GK-0.6 alloys in the peak-aged state, respectively. The d_t and t_t of β' particles of the GK and GK-0.6 alloys are estimated to be about 49 nm and 5 nm, and 33 nm and 3 nm respectively. Therefore, the contribution of the prismatic plane β' particles to the yield strengths of the GK and GK-0.6 alloys in the peak-aged state through the Orowan mechanism is estimated to be 58 and 105 MPa, respectively. That is, the calculated incremental yield strength of the peak-aged alloy after Ce microalloying is 47 MPa, which corresponds reasonably well to the experimental incremental yield strength (53 MPa). Moreover, Nie et al. [57] found that the aspect ratio of the precipitate influences the strength of the alloy. When the aspect ratio

Table 3 Calculated values of grain boundary strengthening for extruded GK and GK-0.6 alloys

Alloy	Regions	Grain boundary strengthening			
		d/ μm	$\Delta\sigma/\text{MPa}$	f/%	$\Delta\sigma_{gbs}/\text{MPa}$
GK	DRX	6.4	74	73	68
	unDRX	14.1	50	27	
GK-0.6	DRX	6.0	77	85	74
	unDRX	9.8	60	15	

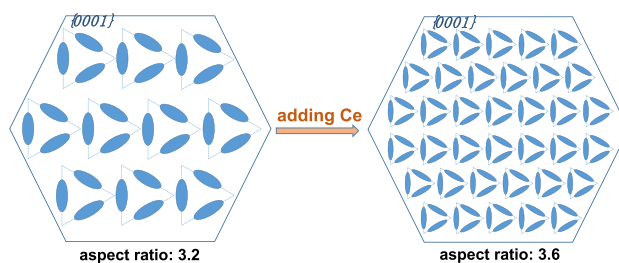


Fig. 16 Schematic diagram of the arrangement of the β' phase of the peak-aged alloy

is enhanced, the β' particles on the prismatic plane form approximately a closed triangular space (Fig. 16). In this closed space, it is difficult for dislocations to escape from the space and cannot continue to move, which further increases the strength of the alloy.

4 Conclusions

The 0.6 wt% Ce was added into Mg–10Gd–0.5Zr alloy, the effect of Ce microalloying on the strength and ductility of wrought Mg–10Gd–0.5Zr alloy was comprehensively investigated, and the strengthening mechanism of Ce microalloying was analyzed and discussed. The following conclusions are reached:

- (1) The addition of 0.6 wt% Ce to the as-cast Mg–10Gd–0.5Zr alloy obviously reduced the grain size and increases the amount of the β -Mg₅Gd eutectic phase.
- (2) Ce microalloying significantly promoted the dynamic recrystallization of the extruded Mg–10Gd–0.5Zr alloy, reducing the size and number of deformed grains, and producing the dynamic precipitation of small amounts of β -Mg₅Gd and α -Mg₁₂Ce particles.
- (3) Ce microalloying weakened the texture of the extruded Mg–10Gd–0.5Zr alloy and transformed the fiber texture of $\langle 10\bar{1}0 \rangle // ED$ into a weak $\langle 0001 \rangle // ED$ abnormal texture.
- (4) The incremental yield strength and ultimate tensile strength of the extruded alloy resulting from Ce microalloying are 14 MPa and 11 MPa respectively, and those of the peak-aged alloy are 53 MPa and 34 MPa respectively. The increase in yield strength of the extruded and peak-aged alloys is ascribed to the enhanced grain boundary strengthening and the promotion of the β' phase precipitation strengthening by Ce microalloying, respectively.

Acknowledgements This work was supported by the National Natural Science Foundation of China (No. 52201119), Central Plains Talent Program-Central Plains Youth Top Talents, China ([2021] 44), and the Natural Science Foundation of Henan Province, China (222300420435).

Declarations

Conflict of interest The authors declare no conflict of interest.

References

1. Z. Zeng, N. Stanford, C.H.J. Davies, J.F. Nie, N. Birbilis, *Int. Mater. Rev.* **64**, 27 (2019)
2. A. Malik, Y. Wang, H. Cheng, F. Nazeer, M.A. Khan, *Res. Eng.* **7**, 100162 (2020)
3. B.C. Suh, M.S. Shim, K.S. Shin, N.J. Kim, *Scr. Mater.* **84–85**, 1 (2014)
4. R.G. Li, J.F. Nie, G.J. Huang, Y.C. Xin, Q. Liu, *Scr. Mater.* **64**, 950 (2011)
5. C. Liu, X. Chen, Y. Hu, W. Zhang, Y. Zhang, J. Li, F. Pan, *J. Mater. Res. Technol.* **21**, 3896 (2022)
6. S. Ouyang, G. Yang, H. Qin, C. Wang, S. Luo, W. Jie, *J. Magnes. Alloy.* **10**, 3459 (2022)
7. J. Zhang, S. Liu, R. Wu, L. Hou, M. Zhang, *J. Magnes. Alloy.* **6**, 277 (2018)
8. H.R.J. Noddooshan, W. Liu, G. Wu, Y. Rao, C. Zhou, S. He, W. Ding, R. Mahmudi, *Mater. Sci. Eng. A* **615**, 79 (2014)
9. Z. Yan, Q. Yang, R. Ma, S. Lv, X. Wu, X. Liu, J. Zhang, C. Yao, F. Meng, X. Qiu, *Mater. Sci. Eng. A* **831**, 142264 (2022)
10. M. Yuan, C. He, J. Zhao, H. Yang, Y. Song, B. Lei, X. Qian, Z. Dong, Q. Li, B. Jiang, F. Pan, *J. Mater. Res. Technol.* **15**, 2518 (2021)
11. T. Homma, N. Kunito, S. Kamado, *Scr. Mater.* **61**, 644 (2009)
12. B. Li, B.G. Teng, D.G. Luo, *Acta Metall. Sinica Engl. Lett.* **31**, 1009 (2018)
13. S.V. Dobatkin, L.L. Rokhlin, E.A. Lukyanova, M.Y. Murashkin, T.V. Dobatkina, N.Y. Tabachkova, *Mater. Sci. Eng. A* **667**, 217 (2016)
14. P. Minárik, J. Veselý, R. Král, J. Bohlen, J. Kubásek, M. Janeček, J. Stráská, *Mater. Sci. Eng. A* **708**, 193 (2017)
15. F. Zhang, K. Zhang, C. Tan, X. Yu, H. Ma, F. Wang, H. Cai, *T. Nonferr. Metal. Soc.* **21**, 2140 (2011)
16. L. Tang, C. Liu, Z. Chen, D. Ji, H. Xiao, *Mater. Des.* **50**, 587 (2013)
17. B. Li, B. Teng, G. Chen, *Mater. Sci. Eng. A* **744**, 396 (2019)
18. Y. Wan, B. Tang, Y. Gao, L. Tang, G. Sha, B. Zhang, N. Liang, C. Liu, S. Jiang, Z. Chen, X. Guo, Y. Zhao, *Acta Mater.* **200**, 274 (2020)
19. X. Liu, X. Chen, J. Li, C. Liu, D. Zhao, R. Cheng, F. Pan, *Prog. Nat. Sci. Mater. Int.* **30**, 213 (2020)
20. C. Huang, C. Liu, S. Jiang, Y. Wan, *J. Alloys Compd.* **874**, 159825 (2021)
21. Y. Du, M. Zheng, B. Jiang, *Vacuum* **151**, 221 (2018)
22. J.S. Li, M.X. Li, Z.M. Hua, Z.T. Hu, H.Y. Wang, *J. Mater. Res. Technol.* **19**, 3088 (2022)
23. B. Li, K. Guan, Q. Yang, X. Niu, D. Zhang, Z. Yu, X. Zhang, Z. Tang, *J. Meng, J. Alloys Compd.* **763**, 120 (2018)
24. A.A. Luo, R.K. Mishra, A.K. Sachdev, *Scr. Mater.* **64**, 410 (2011)
25. M. Masoumi, M. Pegguleryuz, *Mater. Sci. Eng. A* **529**, 207 (2011)
26. L.B. Tong, M.Y. Zheng, S.W. Xu, S. Kamado, Y.Z. Du, X.S. Hu, K. Wu, W.M. Gan, H.G. Brokmeier, G.J. Wang, X.Y. Lv, *Mater. Sci. Eng. A* **528**, 3741 (2011)
27. X. Cui, W. Fu, D. Fang, G. Bi, Z. Ren, S. Guo, S. Li, X. Ding, J. Sun, *J. Mater. Sci. Technol.* **66**, 64 (2021)
28. M. Yang, F. Pan, L. Cheng, J. Shen, *Mater. Sci. Eng. A* **512**, 132 (2009)
29. Y.Z. Du, X.G. Qiao, M.Y. Zheng, K. Wu, S.W. Xu, *Mater. Sci. Eng. A* **620**, 164 (2015)
30. N. Hort, Y. Huang, K.U. Kainer, *Adv. Eng. Mater.* **8**, 235 (2006)
31. M. Hisa, J.C. Barry, G.L. Dunlop, *Philos. Mag. A* **82**, 497 (2002)
32. J.F. Nie, *Metall. Mater. Trans. A* **43**, 3891 (2012)
33. K.Y. Zheng, J. Dong, X.Q. Zeng, W.J. Ding, *Mater. Sci. Technol.* **24**, 320 (2008)
34. Q. Peng, Y. Huang, J. Meng, Y. Li, K.U. Kainer, *Intermetallics* **19**, 382 (2011)
35. S.M. Zhu, J.F. Nie, M.A. Gibson, M.A. Easton, *Scr. Mater.* **77**, 21 (2014)
36. A. Rezaei, R. Mahmudi, C. Cayron, R.E. Loge, *Mater. Sci. Eng. A* **802**, 140616 (2021)

37. A. Hadadzadeh, F. Mokdad, M.A. Wells, D.L. Chen, *Mater. Sci. Eng. A* **709**, 285–289 (2018)
38. A. Imandoust, C.D. Barrett, A.L. Oppedal, W.R. Whittington, Y. Paudel, E. Kadiri, *Acta Mater.* **138**, 27 (2017)
39. J.D. Robson, D.T. Henry, B. Davis, *Acta Mater.* **57**, 2739 (2009)
40. H. Yu, B. Hyuk Park, Y. Sun You, H. Min Kim, Yu. Shun, S. Soo Park, *Mater. Sci. Eng. A* **583**, 25 (2013)
41. S. Lyu, R. Zheng, W. Xiao, Y. Huang, S. Gavras, N. Hort, G. Li, C. Ma, *Mater. Sci. Eng. A* **760**, 426 (2019)
42. R. Alizadeh, R. Mahmudi, A.H.W. Ngan, T.G. Langdon, *Adv. Eng. Mater.* **18**, 1044 (2016)
43. X. Jin, W. Xu, Z. Yang, C. Yuan, D. Shan, B. Teng, B.C. Jin, *J. Mater. Sci. Technol.* **45**, 133 (2020)
44. S.H. Kim, J.G. Jung, B.S. You, S.H. Park, *J. Alloys Compd.* **695**, 344 (2017)
45. Y.N. Wang, J.C. Huang, *Acta Mater.* **55**, 897 (2007)
46. X. Zhang, D. Kevorkov, I.H. Jung, M. Pekguleryuz, *J. Alloys Compd.* **482**, 420 (2009)
47. J.F. Nie, X. Gao, S.M. Zhu, *Scr. Mater.* **53**, 1049 (2005)
48. L.Y. Wei, G.L. Dunlop, H. Westengen, *J. Mater. Sci.* **31**, 387 (1996)
49. C.H. Cáceres, D.M. Rovera, *J. Light Metals* **1**, 151 (2001)
50. N. Hansen, *Scr. Mater.* **51**, 801 (2004)
51. H. Takahashi, Y. Oishi, K. Wakamatsu, N. Kawabe, *Mater. Sci. Forum.* **419–422**, 345 (2003)
52. B.Q. Han, D.C. Dunand, *Mater. Sci. Eng. A* **277**, 297 (2000)
53. M.H. Yoo, *Metall. Trans. A* **12**, 409 (1981)
54. D. Zhang, D. Zhang, F. Bu, X. Li, B. Li, T. Yan, K. Guan, Q. Yang, X. Liu, J. Meng, *J. Alloys Compd.* **728**, 404 (2017)
55. W. Yuan, S.K. Panigrahi, J.Q. Su, R.S. Mishra, *Scr. Mater.* **65**, 994 (2011)
56. K. Guan, Q. Yang, F. Bu, X. Qiu, W. Sun, D. Zhang, T. Zheng, X. Niu, X. Liu, J. Meng, *Mater. Sci. Eng. A* **703**, 97 (2017)
57. J.F. Nie, *Scr. Mater.* **48**, 1009 (2003)
58. J.D. Robson, C. Paa-Rai, *Acta Mater.* **95**, 10 (2015)

Publisher's Note Springer Nature remains neutral with regard to jurisdictional claims in published maps and institutional affiliations.

Springer Nature or its licensor (e.g. a society or other partner) holds exclusive rights to this article under a publishing agreement with the author(s) or other rightsholder(s); author self-archiving of the accepted manuscript version of this article is solely governed by the terms of such publishing agreement and applicable law.